

Multiscale Graph Reduction for Heterogeneous and Anisotropic Discrete Diffusion Processes

Maria Vasilyeva ^{*} James Brannick [†] Ben S. Southworth [‡]

October 14, 2025

Abstract

We present multiscale graph-based reduction algorithms for upscaling heterogeneous and anisotropic diffusion problems. The proposed coarsening approaches begin by constructing a partitioning of the computational domain into a set of balanced local subdomains, resulting in a standard type of domain decomposition. Given this initial decomposition, general coarsening techniques based on spectral clustering are applied within each subgraph in order to accurately identify the key microscopic features of a given system. The spectral clustering algorithm is based on local generalized eigen-decompositions applied to the signed graph Laplacian. The resulting coarse-fine splittings are combined with two variants of energy-minimizing strategies for constructing coarse bases for diffusion problems. The first is an unconstrained minimization formulation in which local harmonic extensions are applied column-wise to construct multi-vector preserving interpolation in each region, whereas the second approach is a variant of the constrained energy minimization formulations derived in the context of non-local multi-continua upscaling techniques. We apply the resulting upscaling algorithms to a variety of tests coming from the graph Laplacian, including diffusion in the perforated domain, channelized media, highly anisotropic settings, and discrete pore network models to demonstrate the potential and robustness of the proposed coarsening approaches. We show numerically and theoretically that the proposed approaches lead to accurate coarse-scale models.

1 Introduction

Diffusion processes in heterogeneous and anisotropic media arise in many applications, including subsurface flow, composite materials, and image and data analysis. Solving the resulting discrete systems becomes particularly challenging when the diffusion coefficient varies strongly or exhibits anisotropy, often spanning several orders of magnitude across the domain. This variability increases the complexity of the resulting linear systems, making them harder to solve efficiently. To reduce the system size and computational cost, various upscaling and multiscale methods have been developed, which yield smaller, coarse-scale systems. Among these, domain decomposition, multiscale, and multigrid methods are widely used, often demonstrating high efficiency. Numerous strategies for constructing a local basis (interpolation) have been developed for heterogeneous problems, mostly in the context of standard (uniform) coarsening. To compensate for this simple coarsening, one generally uses energy minimization techniques or spectral methods since these approaches generate local harmonic bases that can to some degree account for the use of coarse variables that do not align with the heterogeneity or anisotropy for the given problem. From an application standpoint, graph-based physical modeling has traditionally relied on homogenization and upscaling techniques [1, 2]. Recent advances improve local accuracy through multiscale methods, including mortar coupling of network

^{*}Department of Mathematics & Statistics, Texas A& M University - Corpus Christi, Corpus Christi, TX, USA. Email: maria.vasilyeva@tamucc.edu.

[†]Department of Mathematics, The Penn State University, University Park, PA, USA. Email: jjb23@psu.edu.

[‡]Theoretical Division, Los Alamos National Laboratory, NM, USA. Email: southworth@lanl.gov.

and continuum models [3] and the heterogeneous multiscale method [4]. In [5], coarsening for a mixed form of the Laplacian has shown promise in applications to continuum-scale reservoir simulations. Localized orthogonal decomposition has also been explored for fiber-based materials [6, 7]. However, most multiscale methods still assign a single macroscopic variable per local subdomain and rely on structured coarse grids, which limits their effectiveness in complex networks.

This paper develops Multiscale Graph Reduction (MsGR) techniques for coarsening such diffusion processes on heterogeneous and anisotropic structures. To capture the complex discrete structure of the materials, the method introduces local communities with distinct local behavior that are identified using spectral clustering techniques applied within subdomains. The initial subdomains are constructed as in domain decomposition and spectral AMG methods using, for example, METIS [8]. In the proposed scheme, the clustering is derived in each subdomain using a local generalized eigen-decomposition involving the signed graph Laplacian and its diagonal. We emphasize that using the signed graph Laplacian is a purely algebraic way to construct local definite matrices on subdomains or aggregates. Unlike traditional local spectral models that make use of multiple abstract basis functions on each subdomain, our approach assigns explicit macroscopic variables to dominant modes identified via the local spectral problems. We consider two approaches for constructing multiscale basis functions and the corresponding prolongation operators. The first is the CF-approach, which selects centroids of the clusters within subdomains as coarse nodes and builds the interpolation operator using node splitting and a label propagation scheme (i.e., ideal interpolation). The second approach is the MC-algorithm, where local communities (clusters) are treated as coarse variables, and basis functions are obtained by solving local constrained energy minimization problems that capture the average behavior within each local community.

The organization of this paper is as follows. In Section 2, we introduce the weighted graph Laplacian and present different discrete formulations for the anisotropic and diffusive processes. In Section 3, we present the construction of the coarse-scale model, which is based on domain decomposition and local spectral clustering. The numerical results are presented in Section 4 for multiple challenging problems, including (i) graph representations arising from finite element discretizations of heterogeneous perforated media; (ii) highly anisotropic heat flow, and (iii) high-contrast pore network model. The paper ends with a conclusion.

2 Problem formulation

The aim of this paper is to design multiscale graph reduction (MsGR) algorithms for coarsening and upscaling. The methods are based on constructing local weighted graph Laplacians, and using these graph-based representations of the problem to implement aggregation, partitioning, and spectral methods that can be used to coarsen a variety of discrete models. We consider coarsening two forms of heterogeneous and anisotropic diffusion problems: (i) a classical finite element formulation, derived from a continuous diffusion model (elliptic equation), and (ii) a discrete graph model based on the pore network framework [9].

2.1 An elliptic model problem.

The traditional formulation of the diffusion model is given by the elliptic problem

$$-\nabla \cdot (K(x)\nabla u) = q \quad \text{in } \Omega, \quad (1)$$

with Dirichlet boundary conditions

$$u = g \quad \text{on } \partial\Omega, \quad (2)$$

where q is the given source term and K is a symmetric, positive-definite tensor field that may vary spatially and exhibit strong anisotropy or heterogeneity, and the computational domain is denoted by Ω (for example, see Figure 1).

To approximate this problem numerically, we use a standard conforming finite-dimensional subspace $V_h \subset H_0^1(\Omega)$, consisting of piecewise linear functions defined on a mesh \mathcal{T}_h . The finite element approximation

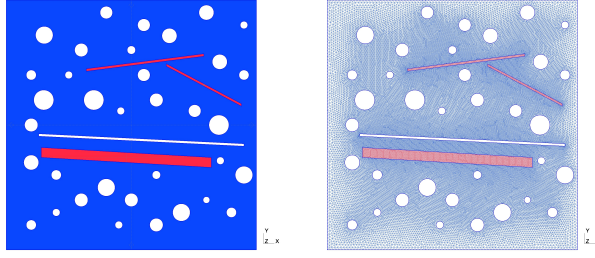


Figure 1: Example heterogeneous perforated domain Ω (right) and mesh \mathcal{T}_h (left).

seeks $u_h \in V_h$ such that

$$\int_{\Omega} K \nabla u_h \cdot \nabla v_h \, dx = \int_{\Omega} q v_h \, dx, \quad \forall v_h \in V_h.$$

Let $\{\phi_i\}_{i=1}^n$ denote the linear basis functions of V_h . Then, the approximate solution can be expressed as

$$u_h(x) = \sum_{j=1}^n u_j \phi_j(x),$$

and the variational problem reduces to a linear system

$$Au = f,$$

where $A \in \mathbb{R}^{n \times n}$ is the stiffness matrix, $u \in \mathbb{R}^n$ is the vector of unknown nodal values, and $f \in \mathbb{R}^n$ is the load vector. The entries of A and f are given by

$$A = \{a_{ij}\}, \quad a_{ij} = \int_{\Omega} K \nabla \phi_j \cdot \nabla \phi_i \, dx, \quad f = \{f_i\}, \quad f_i = \int_{\Omega} q \phi_i \, dx$$

where $\{\phi_i\}$ are the basis functions of V_h .

For the special case of free flux boundary conditions, first order elements, and isotropic $K(x) = 1$, we can interpret the finite element stiffness matrix exactly as a weighted graph Laplacian. More generally, we associate a graph and corresponding weight matrix to the off-diagonal entries in the stiffness matrix, with the graph structure induced by the connectivity of the finite element basis functions and vertices for \mathbb{P}_1 elements. Then $G = (\mathcal{V}, \mathcal{E})$ is a signed undirected graph, on which we define a weighted graph Laplacian $L \in \mathbb{R}^{n \times n}$, where

$$L_{ij} = \begin{cases} \sum_{k \in \mathcal{N}(i)} |a_{ik}|, & \text{if } i = j, \\ -a_{ij}, & \text{if } (i, j) \in \mathcal{E}. \end{cases} \quad (3)$$

The edge weights reflect the anisotropic and heterogeneous properties of the tensor $K(x)$. A key part of utilizing local spectral problems is imposing some sort of natural boundary condition, while maintaining definiteness of the local matrices. If one utilizes element information, this can be assembled directly as in, e.g., the Generalized Multiscale Finite Element Method (GMsFEM) [10, 11] or element-based AMG [12]. Algebraic approaches are more complex and can be posed a finding a symmetric positive semi-definite (SPSD) splitting [13]. Here, we recognize the signed graph Laplacian as a simple method to maintain proper off-diagonal structure and ensure definiteness. Although local signed graph Laplacians sacrifice the splitting property of local matrices to the global matrix as in [13], in the context of identifying coarse variables we find it to be a fast and robust fully algebraic approach.

2.2 Discrete pore network model

The pore network model (PNM) that we consider is a computational framework for simulating flow and transport processes in porous media by representing the complex geometry of a porous matrix as a graph/network structure [9, 14]. In PNM, the pore space is represented as a network of interconnected nodes, where mass conservation equations are defined over the network to simulate multiphase flow and transport processes. The geometry and connectivity of the network are typically extracted from high-resolution imaging (e.g., micro-CT), and flow between pores relates local conductance to pore geometry and fluid properties. In Figure 2, we generate multiple images of different scales, combine them, and apply a network generation algorithm from the openpnm library to extract a multiscale pore network [15].

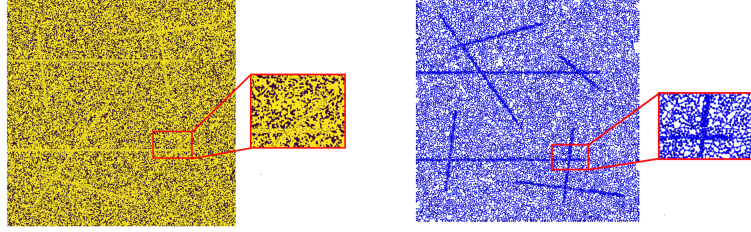


Figure 2: Pore-scale structure with two scales and corresponding high-contrast network

The pore network model can be represented as a weighted undirected graph $G = (\mathcal{V}, \mathcal{E})$, where each node $i \in \mathcal{V}$ corresponds to a pore body at position x_i and each edge $(i, j) \in \mathcal{E}$ represents a throat connecting the two pores with weight $w_{ij} \geq 0$. Therefore, the system of flow equations (mass balance) can be written using the weighted graph Laplacian matrix $L \in \mathbb{R}^{n \times n}$ defined as in (3), where $n = |\mathcal{V}|$ is the number of pores.

Here, each throat (edge) is assigned a hydraulic conductance $w_{ij} \geq 0$, which characterizes its ability to transmit fluid between adjacent pores i and j . For a Newtonian fluid, assuming laminar flow and a circular cross-section, the conductance is typically given by the Hagen–Poiseuille law [9, 16, 6]

$$w_{ij} = \frac{\pi r_{ij}^4}{8\mu l_{ij}},$$

where r_{ij} is the radius of the throat, l_{ij} is the length of the throat, and μ is the dynamic viscosity of the fluid. We note that in this setting the weight matrix W is assumed to be non-negative and, thus, the resulting approximation results in the standard (unsigned) weighted graph Laplacian system.

In the pore network model, the analogue of a Robin boundary condition is imposed in a pointwise manner at boundary nodes. If $\mathcal{V}_{\text{bdy}} \subset \mathcal{V}$ denotes the set of boundary vertices and $\alpha_i \geq 0$ the Robin parameter, then at a boundary node $i \in \mathcal{V}_{\text{bdy}}$ we have

$$(Au)_i = (Lu)_i + \alpha_i u_i = b_i + \alpha_i g = f_i,$$

and for the interior nodes $i \in \mathcal{V} / \mathcal{V}_{\text{bdy}}$

$$(Lu)_i = b_i,$$

where u_i is the pressure at pore i and b_i encodes the source/sink terms. Equivalently, the weighted graph Laplacian is modified by adding a diagonal contribution on boundary nodes:

$$A = L + B, \quad B_{ii} = \begin{cases} \alpha_i, & i \in \mathcal{V}_{\text{bdy}}, \\ 0, & i \in \mathcal{V} \setminus \mathcal{V}_{\text{bdy}}. \end{cases} \quad (4)$$

and f are incorporated boundary conditions and source term.

3 MsGR: Multiscale Graph Reduction

Upscaling and multiscale methods use an aggressive coarsening strategy to construct a relatively small coarse model of the underlying processes [17, 18]. For example, a uniform coarse grid is often utilized in upscaling/multiscale methods, which is also used in the geometric multigrid setting. Furthermore, upscaling and multiscale methods are based on solving local problems: in representative volumes for periodic media, and in each local subdomain for the non-periodic case. In practice, one is interested in equally sized local domains for load-balanced calculations, where a balanced grid partition is usually connected with parallel computations and domain decomposition methods.

In this paper, we propose a coarsening strategy that includes local spectral clustering to define local communities within each subdomain. We use the clusters to enrich the multiscale space, as opposed to using the entire subdomain. As a result, the coarse degrees of freedom and resulting bases capture the complex microscale behavior, can be used with aggressive coarsening to obtain a physically meaningful coarse-scale graph representation, and typically lead to significantly lower complexities when compared to using multiple basis functions with supports on the complete subdomain.

The overall approach we propose is closely related to the multicontinuum theory that has been developed for high-contrast media in the context of the GMsFEMs [10, 11] and to the spectral AMG method originally introduced in [19], but with a refined coarsening strategy and approach for constructing the supports of coarse basis functions. Generally, the MsGR approach can be seen as a hybrid approach that combines ideas from domain decomposition and AMG methods. In terms of domain decomposition, MsGR refines the subdomains by forming clusters within each subdomain, thereby partitioning and adapting the subdomains in a way that captures local heterogeneity and anisotropy. And with respect to AMG coarsening, our approach both localizes the AMG coarsening process, restricting it to subdomains that preserve the mesh features locally, and refines AMG coarsening, which typically relies on heuristics based on the size of the matrix entries to define maximal independent set algorithms used in coarsening.

3.1 Graph partitioning and local domains

Similar to domain decomposition methods, we propose using graph partitioning algorithms like METIS [8] or SCOTCH [20] to form the initial set of subdomains. These algorithms are designed to minimize the interface size between subdomains while maintaining a balance in subdomain sizes and the mesh topology locally within the subdomains.

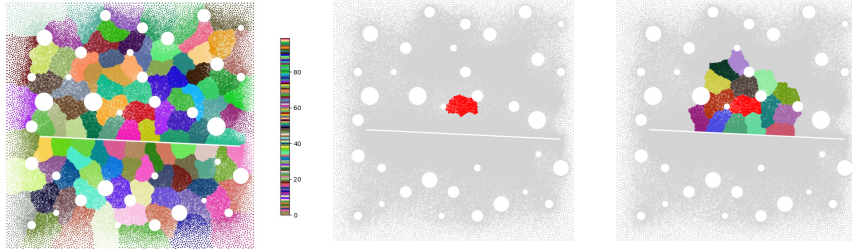


Figure 3: Graph partitioning and local domains Ω_k with $N_\Omega = 100$ (left). Illustration of oversampled subdomain Ω_k^+ . Target subdomain Ω_k (middle) and oversampled subdomains Ω_k^+ based on distances δ_H (right). Red color is used for target subdomain Ω_k

The proposed MsGR algorithm begins with a partition of the graph $G = (\mathcal{V}, \mathcal{E})$ into N_Ω disjoint subdomains

$$\bigcup_{k=1}^{N_\Omega} \Omega_k = \mathcal{V}, \quad \Omega_k \cap \Omega_\ell = \emptyset \quad \text{for } k \neq \ell.$$

Each subdomain $\Omega_k \subset \mathcal{V}$ defines a corresponding subgraph $G_k = (\Omega_k, \mathcal{E}_k)$, where \mathcal{E}_k is the set of edges with both endpoints in Ω_k :

$$G_k = (\Omega_k, \mathcal{E}_k), \quad \mathcal{E}_k = \{(u, v) \in \mathcal{E} \mid u, v \in \Omega_k\}.$$

In Figure 3, we plot a balanced graph partition of 100 subdomains. We used PyMetis (Python wrapper for the METIS library [8]) for partitioning in this example. The DOFs correspond to the triangulation of the perforated domain constructed using the Gmsh library [21], and the mesh contains 80,746 cells, 122,012 edges, and 41,231 nodes. The partitioning to $N_\Omega = 100$ subdomains generates subdomains of size $n^{\Omega_k} = |\Omega_k| \approx 412$ (min=400, max=424).

To capture local interactions beyond Ω_k , we define an oversampled region Ω_k^+ by including all neighboring subdomains that contain nodes within a prescribed physical distance $\delta_H > 0$ from any node in Ω_k . Letting $\text{dist}(u, v)$ denote the Euclidean distance between nodes u and v , the oversampled region is defined as

$$\Omega_k^+ := \Omega_k \cup \{v \in \mathcal{V} \setminus \Omega_k \mid \exists u \in \Omega_k \text{ such that } \text{dist}(u, v) \leq \delta_H\}.$$

The corresponding oversampled subgraph is then defined as

$$G_k^+ = (\Omega_k^+, \mathcal{E}_k^+), \quad \text{where } \mathcal{E}_k^+ = \{(u, v) \in \mathcal{E} \mid u, v \in \Omega_k^+\}.$$

The oversampling procedure is a key step in defining local multiscale basis functions by localizing calculations and preserving the sparsity of the prolongation operator. In Figure 3, we plot subdomain Ω_k (red color) and the corresponding oversampled subdomains Ω_k^+ for $\delta_H = 0.1$.

3.2 Local spectral clustering and multiple coarse-scale variables

Our approach for identifying multiple macroscopic variables in each local subdomain is based on local spectral clustering applied in each of the subdomains, which further partitions the DOFs into communities. For the local network G_k , we consider the localized signed graph Laplacian (3) [22, 23]

$$L^{\Omega_k} = D^{\Omega_k} - W^{\Omega_k}, \quad D^{\Omega_k} = \text{diag}(d_1, \dots, d_{n^{\Omega_k}}), \quad d_i = \sum_{j=1}^{n^{\Omega_k}} |w_{ij}|, \quad (5)$$

where L^{Ω_k} , W^{Ω_k} and D^{Ω_k} are the matrices defined on the sub-network G^{Ω_k} and n^{Ω_k} is the number of nodes in Ω_k . Here W^{Ω_k} is the restriction of the global weight matrix W to the subdomain Ω_k . Then, spectral clustering is applied in each of the subgraphs G_k (correspondingly, each of the subdomains Ω_k) using the local generalized eigenvalue problem:

$$L^{\Omega_k} \phi^{\Omega_k} = \lambda^{\Omega_k} D^{\Omega_k} \phi^{\Omega_k}. \quad (6)$$

The local clusters, or aggregates, in MsGR are defined by first choosing M_k eigenvectors $\phi_r^{\Omega_k}$ corresponding to the smallest eigenvalues $\lambda_r^{\Omega_k}$ with $r = 1, \dots, M_k$ in each G_k . We note that for the sub-network G_k , in the special case that the edge weights are all positive, the local matrix L^{Ω_k} is positive semidefinite such that the eigenvalues satisfy $0 = \lambda_1^{\Omega_k} \leq \lambda_2^{\Omega_k} \leq \dots \leq \lambda_{M_k}^{\Omega_k}$ of L^{Ω_k} , i.e., they are all real and nonnegative; additionally, the smallest eigenvalue $\lambda_1^{\Omega_k} = 0$ and its corresponding eigenvector is the constant [24]. Moreover, solving the generalized eigenvalue problem involving D is equivalent to using the normalized signed Laplacian in local spectral clustering. Theoretically, the use of D in the generalized eigenproblem accounts for the scaling used in defining the norms in the convergence analysis of upscaling methods for highly heterogeneous problems (see the Appendix A for details).

Next, we form a matrix of local eigenvectors $\Phi^{\Omega_k} = [\phi_1^{\Omega_k} \dots \phi_{M_k}^{\Omega_k}] \in \mathbb{R}^{n^{\Omega_k} \times M_k}$ and apply k -means [25, 26, 27] to the normalized rows of Φ^{Ω_k} to partition the data into M_k disjoint clusters (aggregates in AMG)

$$\bigcup_{r=1}^{M_k} \mathcal{A}_k^r = \Omega_k, \quad k = 1, \dots, N_\Omega.$$

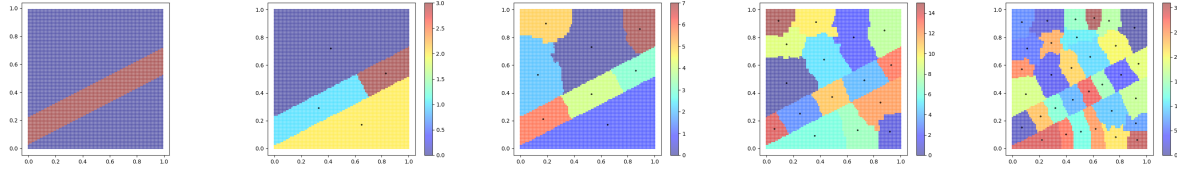


Figure 4: Illustration of spectral clustering and centroids for high-contrast case, $K(x)$ (blue: $K = 1$, red: $K = 10^4$). The first plot displays the coefficient field $K(x)$. The second, third, fourth and fifth plots show the resulting partitions for 4, 8, 16 and 32 clusters.

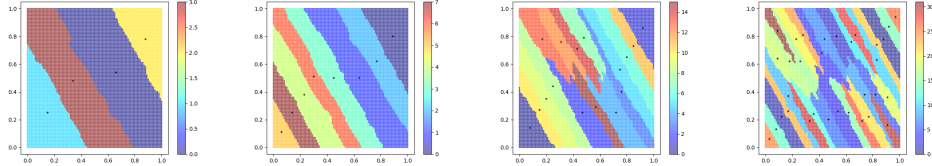


Figure 5: Illustration of local clusters and their centroids for highly anisotropic case. Resulting partitions for 4, 8, 16 and 32 clusters (from left to right).

Here, N_Ω is the number of subdomains generated by METIS and M_k is the number of aggregates in each of the subdomains Ω_k . Once the subdomain nodes have been clustered in the spectral embedding space, we identify representative/coarse points as the centroids μ_j for each cluster. In this work, we define the centroid of each cluster as the geometrically closest data point (in the original space) to the mean of the cluster in the spectral space. We choose the closest point to the centroid $x_c^{\mathcal{A}_k^r}$ of cluster \mathcal{A}_k^r such that

$$x_c^{\mathcal{A}_k^r} = \arg \min_{x_i \in \mathcal{A}_k^r} \|x_i - \mu_r\|_2.$$

This approach ensures that the selected centroid corresponds to an actual node of \mathcal{A}_k^r and provides a meaningful geometric interpretation of the cluster representatives.

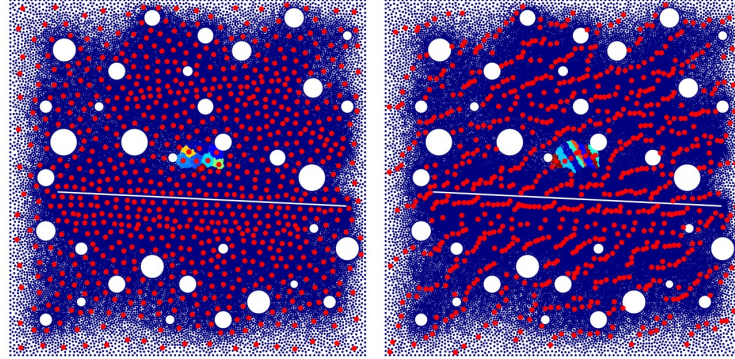


Figure 6: Illustration of local clusters for heterogeneous perforated domain with centroids. Resulting partitions for 8 clusters in isotropic (left) and anisotropic cases (right). In the anisotropic case, note that centroids are narrowly spaced roughly orthogonal to the direction of anisotropy.

In Figure 4, the first plot corresponds to the heterogeneous properties of the scalar spatially varying diffusion coefficient $K(x)$. The second, third, fourth, and fifth plots illustrate the results of spectral clustering,

corresponding to 4, 8, 16, and 32 clusters, respectively. The clusters are depicted with different colors and representative points (centroids). In Figure 5, we plot an illustration of spectral clustering for the fixed highly anisotropic case, $K = R^T DR$, where

$$R = \begin{bmatrix} \cos \theta & -\sin \theta \\ \sin \theta & \cos \theta \end{bmatrix}, \quad D = \begin{bmatrix} d_1 & 0 \\ 0 & d_2 \end{bmatrix}, \quad (7)$$

with $d_1 = 1$, $d_2 = 10^{-4}$ and $\theta = \pi/3$. Last, we consider a more general case involving a domain with heterogeneity, perforations, and potentially anisotropy. The heterogeneous domain consists of two subregions: the main domain (in blue) with permeability $K = 1$, and a highly diffusive channel (in red) with $K = 10^4$ (see the left plot in Figure 1). In addition, we illustrate the effect of anisotropy in the main domain on the formation of local clusters. In Figure 6, we plot local clusters in subdomain Ω_k , and global centroids for isotropic and anisotropic diffusion, with anisotropy as defined in (7). The plots illustrate how spectral clustering based on the given operator understands underlying connections and divides local subdomains into heterogeneity- or anisotropy-aligned clusters. The eigenvectors of the weighted Laplacian encode structural information about the graph, and the spectral embedding reveals approximate block structures corresponding to weakly connected components. These blocks often reflect clusters with minimal interaction between them. Moreover, as seen in Figure 6, since the clusters appropriately align themselves with the heterogeneity or anisotropy, the centroids produce a coarse-fine splitting that accurately captures these features.

3.3 Multiscale basis functions

We consider two approaches for constructing multiscale basis functions and the corresponding prolongation operators within a Galerkin coarsening approach:

- *CF-approach*: Coarse nodes are defined by identifying centroids and using node splitting into disjoint coarse and fine node groups, resulting in a CF-splitting defined in terms of the clustering. Basis functions are computed column-wise as local approximations to ideal interpolation.
- *MC-approach*: Coarse variables are associated with local clusters (aggregates of vertices) and basis functions are computed by solving local constrained energy minimization problems, effectively capturing the average behavior within each community of variables.

Overall, we consider global constructions of these approaches for constructing multiscale basis functions, as well as their corresponding localized versions.

CF-approach

In the *CF-approach*, we partition the node set \mathcal{V} into two disjoint subsets $\mathcal{V} = \mathcal{C} \cup \mathcal{F}$, $\mathcal{C} \cap \mathcal{F} = \emptyset$, where \mathcal{C} denotes the set of coarse nodes and \mathcal{F} the set of fine nodes. In AMG theory, such partitioning is called CF-splitting and plays a fundamental role in constructing the prolongation operator [28, 29]. We start with an approach for deriving the coarse equations based on the global ideal interpolation operator. Given a CF-splitting, ideal interpolation reads

$$P_{ideal} = \begin{bmatrix} \mathcal{W} \\ \mathcal{I} \end{bmatrix}, \quad \mathcal{W} = -A_{\mathcal{F}\mathcal{F}}^{-1} A_{\mathcal{F}\mathcal{C}}, \quad A = \begin{bmatrix} A_{\mathcal{F}\mathcal{F}} & A_{\mathcal{F}\mathcal{C}} \\ A_{\mathcal{C}\mathcal{F}} & A_{\mathcal{C}\mathcal{C}} \end{bmatrix}, \quad (8)$$

where \mathcal{I} is the identity matrix interpolating the coarse variables and \mathcal{W} represents the interpolation weights from the coarse to the fine variables.

After coarsening, we have multiple coarse points (centroids $x_c^{\mathcal{A}_k^r}$) in each subdomain. Define a solution vector over the coarse space $u_{\mathcal{C}} = (u_1^{\Omega_1}, \dots, u_{M_1}^{\Omega_1}, \dots, u_1^{\Omega_{N_{\Omega}}}, \dots, u_{M_{N_{\Omega}}}^{\Omega_{N_{\Omega}}})$, where $u_r^{\Omega_k}$ represents r -th coarse variable in local domain Ω_k , and $u_{\mathcal{C}} \in \mathbb{R}^{n_c}$ for $n_c = \sum_{k=1}^{N_{\Omega}} M_k$. Then let $\psi_r^{\Omega_k} \in \mathbb{R}^n$ denote global multiscale basis functions defined as a column of the global ideal interpolation operator

$$P_{glo} = P_{ideal} = \left[\psi_1^{\Omega_1} \dots \psi_{M_1}^{\Omega_1} \dots \psi_1^{\Omega_{N_{\Omega}}} \dots \psi_{M_{N_{\Omega}}}^{\Omega_{N_{\Omega}}} \right].$$

Recall that, here, N_Ω is the number of local subdomains computed by the MsGR algorithm, and M_k denotes the number of clusters that are computed in each of the subdomains. We can partition our multiscale basis functions across C- and F-points, $\psi_r^{\Omega_k} = (\psi_{r,f}^{\Omega_k}, \psi_{r,c}^{\Omega_k})$. Note by the nature of the identity block in P_{ideal} , we have $\psi_{r,c}^{\Omega_k} = \{e_{r,j}^{\Omega_k}\}$ with $e_{r,\ell(j,b)}^{\Omega_k} = \delta_{ij,rb}$ and index $\ell(j,b)$ corresponding to the centroid $x_c^{\mathcal{A}_j^b}$ of the local cluster \mathcal{A}_j^b , that is, $\psi_{r,c}^{\Omega_k}$ is 1 at the target local cluster centroid $x_c^{\mathcal{A}_k^r}$ and 0 elsewhere. Then, $\psi_r^{\Omega_k} = (A_{\mathcal{FF}}^{-1} A_{\mathcal{FC}} \psi_{r,c}^{\Omega_k}, \psi_{r,c}^{\Omega_k})$. From here we can approximate the fine-grid solution as interpolated from coarse multiscale basis functions via

$$u \approx P_{ideal} u_{\mathcal{C}} = \sum_{k=1}^{N_\Omega} \sum_{r=1}^{M_k} u_r^{\Omega_k} \psi_r^{\Omega_k}.$$

Note, there exists coarse $u_{\mathcal{C}}$ such that this interpolation yields the exact fine-grid solution by nature of linear reduction.

We can localize the above global basis construction and perform calculations in oversampled domains, Ω_k^+ . We define basis functions as follows:

$$\tilde{\psi}_r^{\Omega_k} = (\tilde{\psi}_{r,j}^{\Omega_k}, \tilde{\psi}_{r,c}^{\Omega_k}) = (\mathcal{W}^{\Omega_k^+} \psi_{r,c}^{\Omega_k}, \tilde{\psi}_{r,c}^{\Omega_k}), \quad \mathcal{W}^{\Omega_k^+} = -\left(A_{\mathcal{FF}}^{\Omega_k^+}\right)^{-1} A_{\mathcal{FC}}^{\Omega_k^+}, \quad A^{\Omega_k^+} = \begin{bmatrix} A_{\mathcal{FF}}^{\Omega_k^+} & A_{\mathcal{FC}}^{\Omega_k^+} \\ A_{\mathcal{CF}}^{\Omega_k^+} & A_{\mathcal{CC}}^{\Omega_k^+} \end{bmatrix},$$

where $\tilde{\psi}_{r,c}^{\Omega_k}$ is the vector with zeros in all elements except continuum r in target aggregate \mathcal{A}_k . The operator $A^{\Omega_k^+}$ is the block of the global operator A corresponding to the oversampled domain of the k th aggregate, Ω_k^+ . The local construction of prolongation is then given by

$$P_{loc} = \left[\tilde{\psi}_1^{\Omega_1} \dots \tilde{\psi}_{M_1}^{\Omega_1} \dots \tilde{\psi}_1^{\Omega_{N_\Omega}} \dots \tilde{\psi}_{M_{N_\Omega}}^{\Omega_{N_\Omega}} \right],$$

where $\tilde{\psi}_r^{\Omega_k}$ are the localized basis functions mapped to the global indexing. This procedure is analogous to the approach used in constructing ℓ AIR restriction and interpolation [30, 31, 32], where ideal interpolation (or restriction) is enforced exactly over local overlapping subdomains, and is also used in energy minimization techniques for balancing domain decomposition methods [33]. Using MsGR coarsening with this interpolation can be seen as a refinement to both these AMG and DD approaches.

MC-approach

In the *MC-approach*, coarse variables identified with clusters are considered as a community of nodes that exhibit similar behavior and are represented in an averaged manner, as in unsmoothed aggregation AMG [34]. The method is motivated by the Nonlocal Multicontinua Upscaling (NLMC) method [35, 36, 37], where each constraint corresponds to a specific continuum. However, in NLMC, these constraints must be predefined prior to computation, which is only feasible in simple settings where the continua can be manually identified.

To construct multiscale basis functions associated with subdomain Ω_k in the *MC-approach*, we begin with a global constrained energy minimization problem. Let \mathcal{A}_k^r denote the aggregate associated with the local clusters $r = 1, \dots, M_k$, and assume that $\cup_{r=1}^{M_k} \mathcal{A}_k^r = \Omega_k$. Hence, we have an aggregation for each subdomain. Then, for a fixed pair (k, r) , the basis function $\psi_r^{\Omega_k}$ is obtained by solving:

$$\min_{\psi} \frac{1}{2} \psi^T A \psi \quad \text{subject to} \quad S^{\mathcal{A}_j^b} \psi = \delta_{kj} \delta_{rb}, \quad \forall j = 1, \dots, N_\Omega, \quad b = 1, \dots, M_j, \quad (9)$$

where $S^{\mathcal{A}_j^b}$ represents the constraint operator associated with the aggregate \mathcal{A}_j^b . The Kronecker delta δ_{kj} and δ_{rb} ensures the physical meaning of the basis function with respect to the r -th constraint in Ω_k . The operator $S^{\mathcal{A}_j^b}$ represents the local constraint operator associated with the aggregate \mathcal{A}_j^b . It computes the

mean value of a fine-scale function over the aggregate and enforces the continuum separation conditions. The discrete form of $S^{\mathcal{A}_j^b}$ is given as a row vector with entries 1 or 0

$$S^{\mathcal{A}_j^b} = \{s_i\}, \quad s_i = \begin{cases} 1/n^{\mathcal{A}_j^b}, & \text{if } x_i \in \mathcal{A}_j^b, \\ 0, & \text{otherwise.} \end{cases}$$

where $n^{\mathcal{A}_j^b} = |\mathcal{A}_j^b|$. The constraint equation ensures that the basis function associated with the aggregate \mathcal{A}_k^r has an average value of one over its own aggregate \mathcal{A}_k^r , and zero over all other aggregates \mathcal{A}_j^b within the global domain (graph).

To solve the constrained minimization problem, we apply the method of Lagrange multipliers, leading to the following saddle-point system:

$$\begin{aligned} A\psi_r^{\Omega_k} + \sum_{j=1}^{N_\Omega} \sum_{b=1}^{M_j} (S^{\mathcal{A}_j^b})^T \gamma_{b,j} &= 0, \\ S^{\mathcal{A}_j^b} \psi_r^{\Omega_k} &= \delta_{kj} \delta_{rb}, \quad \forall \mathcal{A}_j^b, \end{aligned} \tag{10}$$

where $\gamma_{b,j}$ are the Lagrange multipliers associated with the constraints imposed on the aggregate \mathcal{A}_j^b .

For a localized approach, we construct a set of basis functions $\tilde{\psi}_r^{\Omega_k} \in \Omega_k^+$ by solving the local problems with zero Dirichlet boundary conditions subject to continuum separation constraints. We solve the following constrained cell problems formulated using Lagrange multipliers

$$\begin{aligned} A^{\Omega_k^+} \tilde{\psi}_r^{\Omega_k} + \sum_{\Omega_j \subset \Omega_k^+} \sum_{\mathcal{A}_j^b \subset \Omega_j} (S^{\mathcal{A}_j^b})^T \gamma_{b,j} &= 0, \\ S^{\mathcal{A}_j^b} \tilde{\psi}_r^{\Omega_k} &= \delta_{kj} \delta_{rb}, \quad \forall \mathcal{A}_j^b \subset \Omega_j \subset \Omega_k^+. \end{aligned} \tag{11}$$

The operator $S^{\mathcal{A}_j^b}$ represents the local constraint operator associated with the aggregate \mathcal{A}_j^b . The constraints give meaning to the coarse scale solution and produce a mean value of one on the coarse aggregate \mathcal{A}_k^r for the current community and zero on all other aggregates within Ω_k^+ .

Finally, we define prolongation operators related to global and localized versions

$$P_{glo} = \left[\psi_1^{\Omega_1} \dots \psi_{M_1}^{\Omega_1} \dots \psi_1^{\Omega_{N_\Omega}} \dots \psi_{M_{N_\Omega}}^{\Omega_{N_\Omega}} \right], \quad P_{loc} = \left[\tilde{\psi}_1^{\Omega_1} \dots \tilde{\psi}_{M_1}^{\Omega_1} \dots \tilde{\psi}_1^{\Omega_{N_\Omega}} \dots \tilde{\psi}_{M_{N_\Omega}}^{\Omega_{N_\Omega}} \right],$$

where $\psi_r^{\Omega_k}$ are the global basis functions and $\tilde{\psi}_r^{\Omega_k}$ the localized multiscale basis functions mapped to the global indexing.

3.4 Coarse-scale system

To define a coarse grid approximation of steady-state system $Au = f$, we use a prolongation matrix $P \in \mathbb{R}^{n_c \times n}$ and form a coarse-grained system as follows

$$A_c u_c = f_c, \quad A_c = RAP \in \mathbb{R}^{n_c \times n_c}, \quad f_c = Rf \in \mathbb{R}^{n_c}, \tag{12}$$

where we set $R = P^T \in \mathbb{R}^{n \times n_c}$ for the restriction operator for symmetric problems. Moreover, we can reconstruct the fine-scale solution

$$u_{ms} := Pu_c \in \mathbb{R}^n.$$

We note that the error depends on the partitioning into subdomains Ω_k (H) and intra-cluster heterogeneity C_{ratio} (contrast ratios within local cluster)

$$\|u - u_{ms}\|_A = \mathcal{O}\left(H C_{ratio}^{1/2}\right).$$

where $H = \max_{k,r} H_{k,r}$, $H_{k,r} = \text{diam}(\mathcal{A}_k^r)$, $C_{ratio} = \max_{k,r} C_{ratio}^{k,r}$, $C_{ratio}^{k,r} = \bar{w}^{r,k}/\underline{w}^{r,k}$ ($\underline{w}^{k,r} \leq w_{ij} \leq \bar{w}^{k,r}$ and w_{ij} is the connection weight of edge $e_{ij} \in \mathcal{G}_k$). Here u is the solution of fine-scale system (4), $u_{ms} = Pu_c$ is the multiscale interpolated solution of (12), and $\|v\|_A^2 = v^T A v$ (see Appendix A for details).

4 Numerical results

To demonstrate the effectiveness of the proposed local spectral clustering approach, we examine three test problems: *(Test 1)* an elliptic equation discretized by finite elements on a heterogeneous perforated domain; *(Test 2)* a highly anisotropic heat flow problem; and *(Test 3)* a high-contrast pore network model. We compare a multiscale solution u_{ms} with reference solution in L_2 ($\|u\|^2 = v^T v$) and energy ($\|v\|_A^2 = v^T A v$) norms

$$e_1 = \frac{\|u - u_{ms}\|}{\|u\|} \times 100\%, \quad e_2 = \frac{\|u - u_{ms}\|_A}{\|u\|_A} \times 100\%,$$

where the relative error is presented in percentage. As a reference solution, we use the fine-scale solution. Implementation is performed using the Python with the SciPy sparse library to represent and solve the resulting system of linear equations. We used PyMetis (Python wrapper for the METIS library [8]) for graph partitioning.

4.1 Test 1: Elliptic problem in heterogeneous perforated domain

We consider a heterogeneous perforated domain $\Omega = [0, 1]^2$ with 35 circular perforations and one thin long perforation in the middle of the domain (see Figure 1). We have heterogeneous coefficient $K(x)$ defined in $\Omega = \Omega_1 \cup \Omega_2$, where we set $K(x) = K_1$ in Ω_1 (main domain) and $K(x) = K_2$ in Ω_2 (channels domain) (see Figure 1, blue and red color represent Ω_1 and Ω_2).

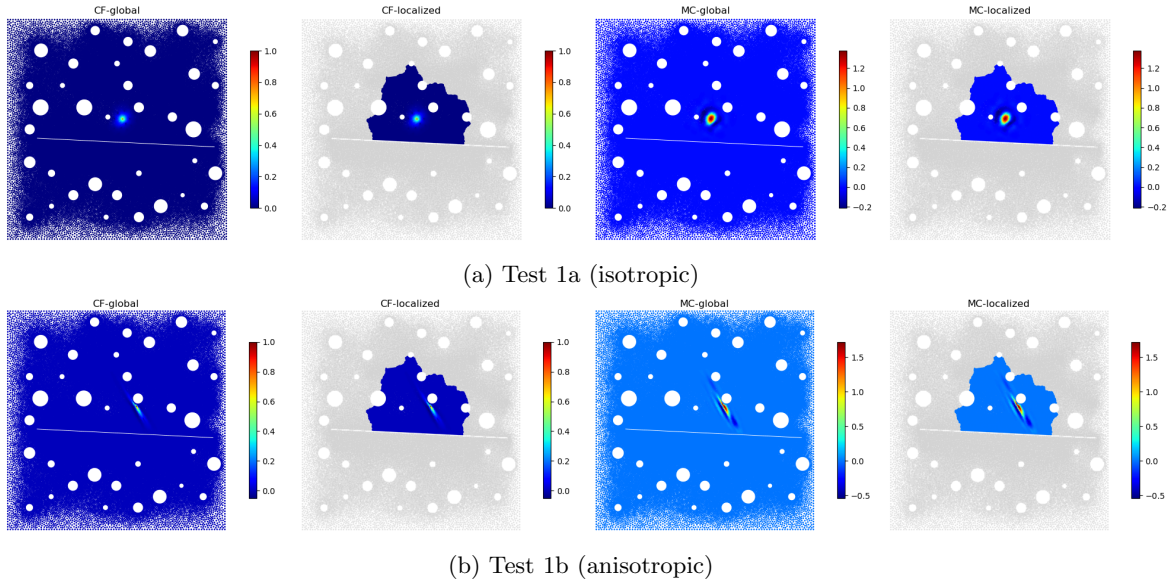


Figure 7: Tests 1a and 1b. Multiscale basis functions (global and local) for CF- and MC-approaches. $N_\Omega = 100$ and $M = 8$

Geometry and triangulation are constructed using the Gmsh library [21]. We use an unstructured locally refined mesh with 80,746 cells, 122,012 edges, and 41,231 nodes. We solve the diffusion problem (1) with zero Dirichlet boundary conditions on all boundaries and set the source term $q = 1$. We consider isotropic and anisotropic backgrounds (k_1). In the isotropic case (*Test 1a*), we set $K_1 = K_{iso} = 1$. In anisotropic case (*Test 1b*), the diffusion tensor $K_1 = K_{aniso} = (R_D)^T D R_D$ is defined by (7) with $d_1 = 1$ and $d_2 = 10^{-4}$ and $\theta = \pi/3$.

Figure 7 shows the multiscale basis functions obtained using the CF and MC approaches with both global and localized constructions. Localization is performed with $\delta_H = 0.1$ (see Figure 3). In Figure 8,

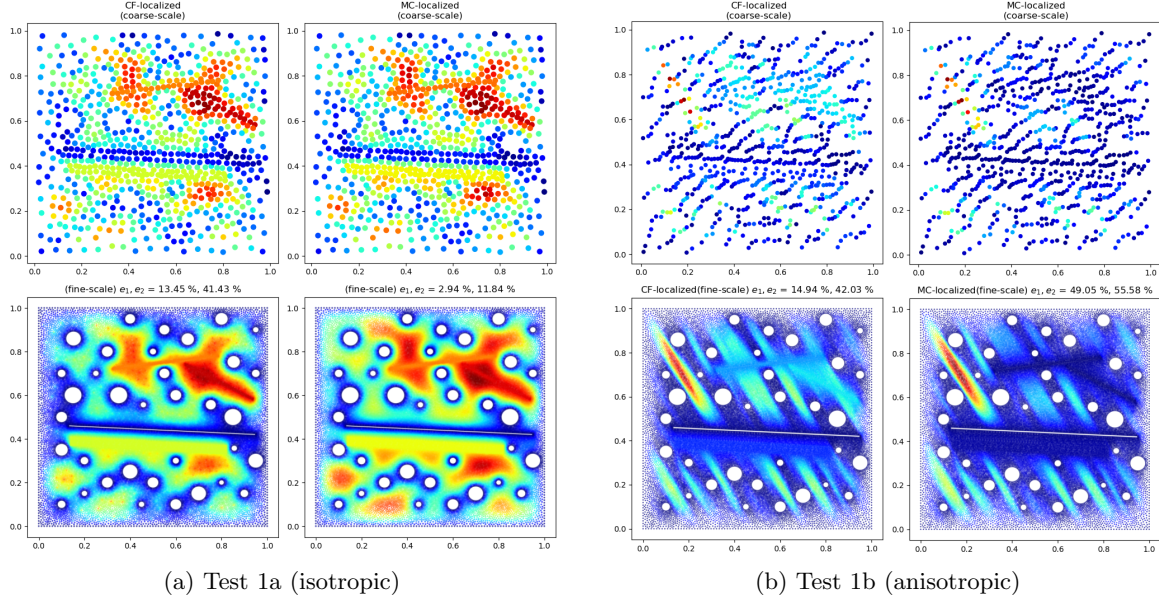


Figure 8: Tests 1a and 1b. Multiscale solution: coarse-scale solution u_c (first row), projected to fine-scale u_{ms} (second row) and after three colored local correction iterations (third row). $DOF_c = 800$ (coarse-scale, $N_\Omega = 100$ and $M = 8$) and $DOF = 41,231$ (fine-scale)

we present the coarse- and fine-scale solutions obtained with localized CF and MC approaches. The first row illustrates the solutions at the coarse degrees of freedom, where the values are shown at the cluster centroids, demonstrating that the coarse models remain physically meaningful. The corresponding coarse graph solutions are then projected onto the fine-scale resolution using the prolongation matrix P , and the results are plotted in the second row. Additionally, the errors e_1 and e_2 are reported.

In Table 1, we present relative errors in %. Localization is performed with $\delta_H = 0.1$ (see Figure 3). We observe the error decay in L_2 and energy norms (e_1 and e_2) with respect to the number of basis functions M corresponding to the number of local clusters, for two settings of $N_\Omega = 25$ and $N_\Omega = 100$ (number of subdomains). Both global (glo) and local (loc) strategies in basis construction are tested for the CF-approach and the MC-approach. As the number of local clusters M increases, the error consistently decreases across all methods, with global construction performing better than the localized version. The larger number of local domains $N_\Omega = 100$ yields significantly improved accuracy, especially for the CF-approach. We see that with larger M , we obtain better localization for basis construction.

4.2 Test 2: Anisotropic heat diffusion

We consider anisotropic diffusion in a domain $\Omega = [0, 1]^2$ for temperature $u = u(x)$

$$-\nabla \cdot q = f, \quad q = k_{\parallel} \nabla_{\parallel} u + k_{\perp} \nabla_{\perp} u,$$

with $\nabla_{\parallel}(\cdot) = (b \cdot \nabla(\cdot))b$ and $\nabla_{\perp} = \nabla - \nabla_{\parallel}$, $b = B/|B|$, where B is the given magnetic field, and k_{\parallel} and k_{\perp} are the heat conductivity parallel and perpendicular to normalized magnetic field lines b , respectively.

Therefore, we solve the following formulation:

$$-\nabla \cdot (k_{\perp} \nabla u) - \nabla \cdot (k_{\Delta} b(b \cdot \nabla u)) = f,$$

with $k_{\Delta} = k_{\parallel} - k_{\perp}$. This is a simplified model for temperature evolution along magnetic fields in magnetic confinement fusion, which remains a very challenging problem due to dynamically evolving non-mesh-aligned anisotropy and anisotropy ratios of 10^{10} or larger, e.g., [38].

M		$N_\Omega = 25$				$N_\Omega = 100$			
		CF		MC		CF		MC	
		e_1	e_2	e_1	e_2	e_1	e_2	e_1	e_2
Test 1a									
1	glo	73.36	86.66	9.76	21.58	44.66	71.17	3.55	11.95
	loc	93.12	96.01	51.61	54.61	84.51	89.31	62.45	57.85
2	glo	49.82	75.24	6.55	17.30	32.89	62.13	2.32	9.29
	loc	90.65	93.88	58.13	57.00	54.85	73.84	53.36	53.26
4	glo	42.84	70.00	3.81	12.62	21.94	51.84	1.41	6.33
	loc	62.99	79.14	51.83	52.32	22.24	52.22	7.66	20.33
8	glo	33.32	62.46	2.06	8.45	13.41	31.37	1.15	4.81
	loc	33.49	62.66	32.53	35.52	13.45	41.43	2.94	11.84
16	glo	23.03	52.78	1.32	5.91	7.14	30.65	1.11	4.34
	loc	23.06	52.82	4.59	15.73	7.14	30.66	1.11	4.34
32	glo	13.95	41.89	1.16	4.79	3.49	21.63	1.04	3.99
	loc	13.95	41.90	5.14	13.94	3.49	21.63	1.04	3.99
Test 1b									
1	glo	78.29	88.08	6.56	16.93	53.04	72.65	2.79	9.67
	loc	91.02	96.12	38.97	52.03	88.37	93.15	51.69	59.27
2	glo	70.59	81.76	5.24	14.51	40.35	63.71	2.12	8.27
	loc	88.84	94.15	41.88	53.38	81.03	88.12	51.27	58.32
4	glo	46.51	69.45	3.73	12.20	23.80	51.73	1.35	6.66
	loc	69.45	84.67	42.01	52.81	59.05	75.33	50.99	57.59
8	glo	36.80	61.89	2.57	10.39	11.74	37.93	0.81	5.62
	loc	42.93	67.85	45.92	54.65	14.94	42.03	49.05	55.58
16	glo	21.12	49.11	1.97	9.02	5.48	26.81	0.41	3.88
	loc	24.67	52.83	46.07	52.68	5.62	27.10	20.31	29.02
32	glo	10.95	36.64	0.91	6.07	2.86	19.28	0.33	3.33
	loc	11.00	36.72	29.71	36.34	2.86	19.29	0.32	3.92

Table 1: Tests 1a and 1b. MsGR with global and localized multiscale basis functions

Homogeneous Dirichlet boundary conditions $u(x) = 0$ are imposed on $\partial\Omega$. We set $f = 0$ and consider $k_{\parallel} = 1.0$ and $k_{\perp} = 10^{-1}$ in *Test 2a* and $k_{\perp} = 10^{-3}$ in *Test 2b*. We use a structured 200×200 mesh with 80,000 cells, 120,400 edges, and 40,401 nodes. Figure 9 shows the multiscale basis functions obtained using the CF and MC approaches with both global and localized constructions. We observe that, in both approaches, the basis functions align with the magnetic field. In Figures 10, we present a multiscale solution in coarse- and fine-scale representations. The first row illustrates the solutions at the coarse degrees of freedom as well as their magnetic field-aligned distribution of centroids (coarse nodes). The corresponding coarse-scale solutions are then projected onto the fine-scale resolution using the prolongation matrix P , and the results are plotted in the second row.

In Table 2, we present relative errors in % for a varying number of basis functions M . We present results for global (glo) and localized basis construction, where we consider local domains corresponding to oversampled local domains Ω_i^+ constructed with $\delta_H = 0.1$ (loc1) and $\delta_H = 0.2$ (loc2). We observe that a larger local domain is needed to achieve good localization due to the strong anisotropy. We see the error decay for different coarse space constructions as the number of multiscale basis functions (local clusters) per local domain increases. The plots compare the CF-approach and the MC-approach with global and localized basis functions for both moderate (Test 2a) and strong (Test 2b) anisotropies. For moderate anisotropy, both methods demonstrate rapid error reduction as M increases. However, as anisotropy becomes larger in Test 2b, the effectiveness of localized methods diminishes for small M , and accurate coarse spaces only

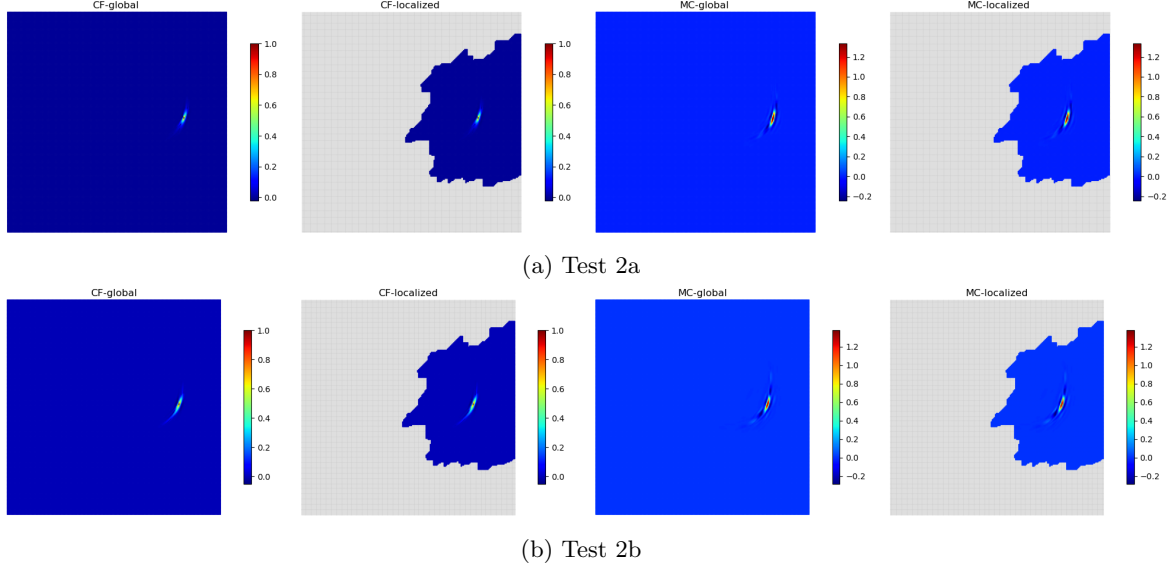


Figure 9: Tests 2a and 2b. Multiscale basis functions (global and local) for CF- and MC-approaches. $N_\Omega = 100$ and $M = 32$

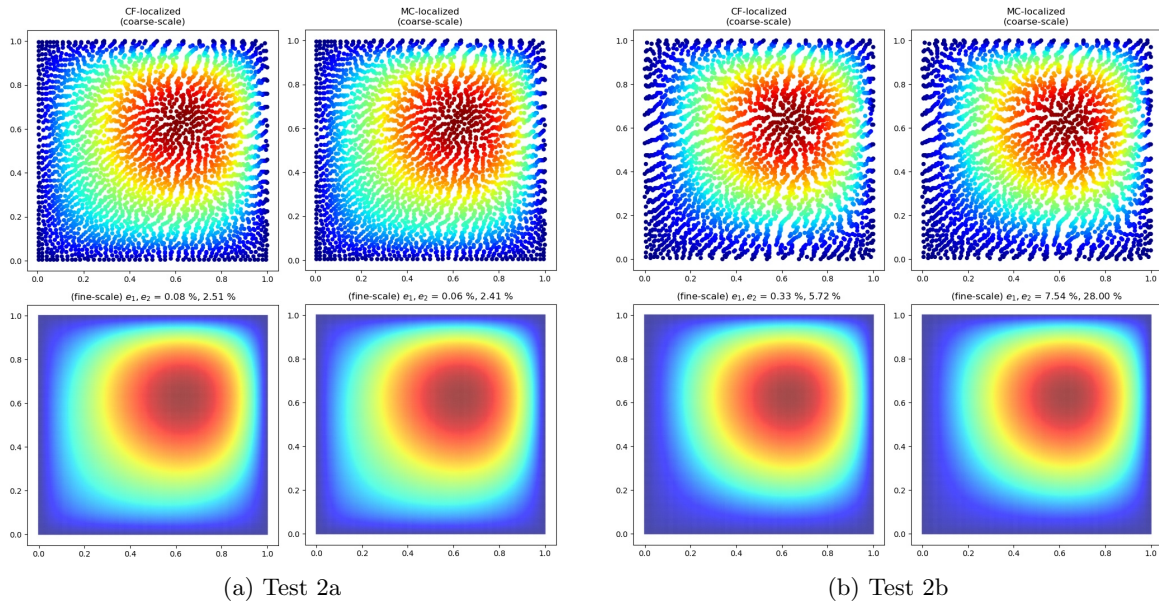


Figure 10: Tests 2a and 2b. Multiscale solution: coarse-scale solution u_c (first row) and projected to fine-scale u_{ms} (second row). $DOF_c = 3, 200$ (coarse-scale, $N_\Omega = 100$ and $M = 32$) and $DOF = 40, 401$ (fine-scale)

emerge when M is sufficiently large and more global information is incorporated by considering a larger oversampled local domain in basis construction. The challenge of resolving highly anisotropic features with localized bases emphasizes the need for a global approach in the extreme anisotropy regime.

M		$N_\Omega = 25$				$N_\Omega = 100$			
		CF		MC		CF		MC	
		e_1	e_2	e_1	e_2	e_1	e_2	e_1	e_2
Test 2a									
1	glo	8.39	30.05	0.01	0.13	2.58	16.08	0.01	0.24
	loc1	97.02	98.41	93.47	95.40	97.28	98.35	93.26	95.35
	loc2	88.54	94.39	73.43	84.05	86.85	92.86	67.87	80.72
2	glo	4.62	21.89	0.01	0.16	1.36	11.35	0.01	0.51
	loc1	95.52	97.48	91.55	94.39	93.50	96.12	88.83	92.87
	loc2	76.27	87.89	61.45	77.20	64.74	80.07	39.28	61.48
4	glo	2.75	16.20	0.01	0.31	0.70	7.93	0.00	0.71
	loc1	90.57	94.83	90.19	93.73	81.60	89.31	83.39	89.97
	loc2	55.06	74.79	50.93	70.01	17.93	42.51	19.86	43.94
8	glo	1.38	11.30	0.01	0.52	0.34	5.46	0.01	0.84
	loc1	73.98	85.46	88.77	93.08	47.22	67.75	75.29	85.37
	loc2	18.17	43.20	36.66	59.82	1.18	11.31	10.52	31.80
16	glo	0.73	7.98	0.00	0.70	0.16	3.71	0.01	0.94
	loc1	33.13	57.27	73.88	84.25	5.24	22.73	52.41	71.38
	loc2	2.51	16.51	16.15	39.94	0.17	3.87	1.16	10.73
32	glo	0.36	5.52	0.01	0.85	0.08	2.51	0.01	1.03
	loc1	3.15	17.96	50.07	69.75	0.09	2.98	20.16	44.28
	loc2	0.42	6.36	7.02	26.33	0.08	2.51	0.06	2.41
Test 2b									
1	glo	0.87	8.46	0.00	0.12	0.30	4.86	0.01	0.82
	loc1	99.36	99.77	99.87	99.82	99.83	99.92	99.88	99.85
	loc2	98.14	99.33	99.66	99.62	99.31	99.71	99.50	99.61
2	glo	0.38	5.53	0.00	0.56	0.24	4.87	0.15	3.79
	loc1	99.88	99.92	99.84	99.79	99.79	99.88	99.81	99.80
	loc2	97.68	99.11	99.37	99.45	99.06	99.56	98.47	99.15
4	glo	0.29	4.76	0.03	1.68	0.27	5.31	0.47	6.70
	loc1	99.52	99.77	99.74	99.75	99.62	99.78	99.73	99.73
	loc2	96.40	98.55	97.98	98.86	97.07	98.68	96.52	98.19
8	glo	0.23	4.58	0.18	4.21	0.31	5.58	0.67	8.05
	loc1	99.32	99.63	99.76	99.75	98.51	99.27	99.64	99.67
	loc2	93.41	97.15	96.97	98.43	83.22	92.36	93.68	96.82
16	glo	0.26	5.18	0.40	6.22	0.33	5.73	0.86	9.15
	loc1	97.66	98.81	99.74	99.74	93.61	96.63	98.94	99.36
	loc2	84.35	92.52	95.21	97.75	5.41	23.44	75.74	87.93
32	glo	0.29	5.42	0.65	7.98	0.33	5.71	1.10	10.34
	loc1	90.70	95.13	98.97	99.40	4.99	22.53	95.17	97.62
	loc2	44.02	66.49	86.38	93.70	0.33	5.72	7.54	28.00

Table 2: Tests 2a and 2b. MsGR with global and localized multiscale basis functions ($\delta_H = 0.1$ for loc1 and 0.2 for loc2)

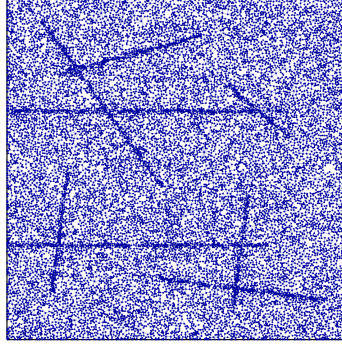
4.3 Test 3: Pore network model

We consider a time-dependent problem on a discrete structure defined by a pore network model, where assign a heterogeneous property c_i for each node that can be associated with the pore volume or fluid compressibility

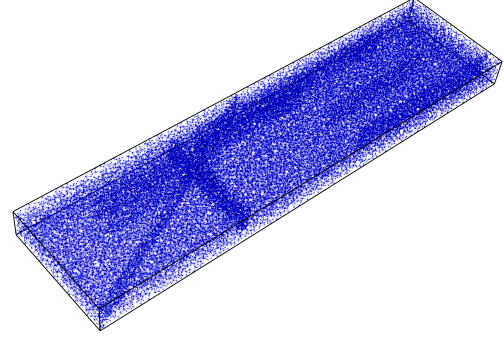
[39]. The mass conservation equation leads to the following parabolic equation

$$Cu_t + Au = f, \quad 0 < t \leq T,$$

where $C = \text{diag}(c_1, \dots, c_n)$ is the diagonal matrix. We set point-source at the two (Test 3a) and one (Test 3b) boundary points connected to channels and consider initial conditions $u = u_0$ at $t = 0$.



(a) Test 3a



(b) Test 3b

Figure 11: Test 3a and 3b. pore network structure

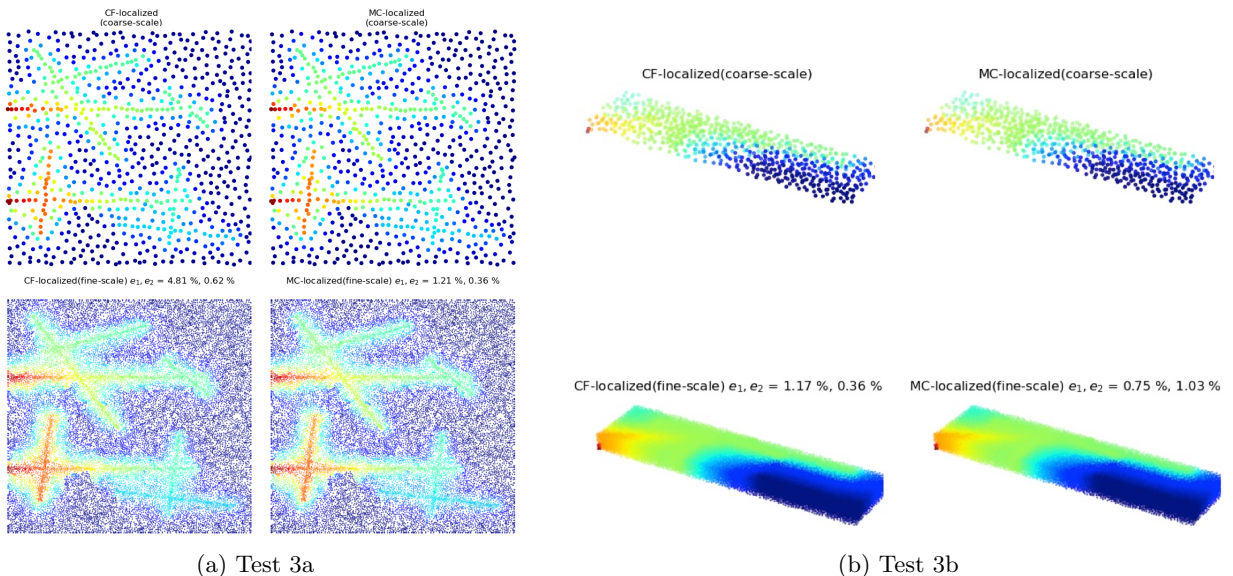


Figure 12: Tests 3a and 3b. Multiscale solution: coarse-scale solution u_c (first row) and projected to fine-scale u_{ms} (second row). Test 3a: $DOF_c = 802$ (coarse-scale, $N_\Omega = 100$ and $M = 8$) and $DOF = 18,983$ (fine-scale). Test 3b: $DOF_c = 801$ (coarse-scale, $N_\Omega = 100$ and $M = 8$) and $DOF = 38,058$ (fine-scale)

To define a coarse grid approximation of unsteady system, we form a coarse-grained system as follows

$$C_c(u_c)_t + A_c u_c = f_c \quad \text{with} \quad A_c = RAP, \quad C_c = RCP, \quad f_c = Rf \quad \text{and} \quad u_{ms} = Pu_c.$$

M		$N_\Omega = 25$				$N_\Omega = 100$			
		CF		MC		CF		MC	
Test 3a									
1	glo	64.95	6.71	18.35	1.89	23.21	2.54	4.62	0.49
	loc	66.09	7.35	54.78	6.33	53.26	6.29	74.39	8.72
2	glo	45.78	4.80	11.10	1.15	15.74	1.77	2.43	0.26
	loc	54.34	6.00	49.75	5.79	30.33	3.63	59.90	7.05
4	glo	26.19	2.83	6.60	0.69	9.60	1.12	0.89	0.10
	loc	26.76	3.03	40.55	4.83	9.60	1.18	32.68	4.00
8	glo	17.89	1.97	3.41	0.36	4.81	0.62	0.29	0.04
	loc	17.80	1.96	8.67	1.38	4.81	0.62	1.21	0.36
16	glo	9.46	1.10	1.03	0.12	2.10	0.32	0.09	0.02
	loc	9.46	1.10	1.14	0.14	2.10	0.32	0.12	0.04
32	glo	4.82	0.62	0.32	0.04	0.96	0.18	0.03	0.01
	loc	4.82	0.62	0.33	0.05	0.96	0.18	0.03	0.01
Test 3b									
1	glo	11.15	2.78	2.20	0.84	5.82	1.17	0.63	0.35
	loc	82.22	30.74	83.06	32.08	82.26	30.73	86.57	33.15
2	glo	7.68	1.51	0.80	0.43	4.11	0.87	0.33	0.23
	loc	81.85	30.74	79.01	30.51	15.82	7.15	71.34	27.51
4	glo	6.29	1.25	0.29	0.22	2.32	0.56	0.10	0.13
	loc	17.47	8.23	52.28	20.49	1.64	0.59	40.90	16.53
8	glo	4.09	0.87	0.22	0.18	1.24	0.38	0.03	0.10
	loc	3.46	1.49	50.01	19.67	1.17	0.36	0.75	1.03
16	glo	2.39	0.57	0.09	0.12	0.56	0.29	0.02	0.14
	loc	2.32	0.56	12.66	6.18	0.56	0.29	0.08	0.28
32	glo	1.25	0.38	0.02	0.09	0.23	0.32	0.02	0.18
	loc	1.24	0.38	0.54	0.84	0.23	0.32	0.03	0.19

Table 3: Tests 3a and 3b. MsGR with global and localized multiscale basis functions

We let τ be an uniform time step size and u^n be a solution at time t^n , where $t^n = \ell\tau$ for $\ell = 1, \dots, N_t$. Then, using the implicit backward Euler approximation for the time derivative, we obtain the following fully discrete coarse-grained system

$$C_c \frac{u_c^{n+1} - u_c^n}{\tau} + A_c^{n+1} u_c^{n+1} = f_c, \quad A_c = RAP, \quad C_c = RCP, \quad f_c = Rf, \quad u_{ms} = Pu_c.$$

with initial condition, $u_c^{n=0} = u_{c,0}$. We simulate for $T = 10^2$ with 20 time steps.

We consider two test cases corresponding to two pore-structures (Figure 11). In Test 3a, the geometry and connectivity of the network are extracted from two images with differing porosity using a network generation algorithm from the openpnm library [15]. The resulting pore network in Test 3a consists of 18,983 nodes and 27,936 connections, corresponding to a structure embedded in a square domain, $[0, 1] \times [0, 0.25] \times [0, 0.065]$. In Test 3b, we have a network with 38,058 nodes and 113,000 connections, corresponding to a structure embedded in a square domain, $[0, 3000]^2$. Connection weights are assigned based on Poiseuille flow through tubes, using the geometric characteristics of the network, with values ranging from $0.0008 \leq w_{ij} \leq 18.85$ in Test 3a and from $0.0016 \leq w_{ij} \leq 46.64$ in Test 3b. For coefficients c_i , the values range from $0.1 \leq c_i \leq 0.82$ in Test 3a and from $0.1 \leq c_i \leq 1$ in Test 3b.

In Figures 12, we present a multiscale solution in coarse- and fine-scale representations. In Table 3, we present relative errors in % for varying number of basis functions M for $N_\Omega = 25$ and 100. We present

relative errors in L_2 (e_1) and energy norm (e_2) at the final time. We observe an error decrease for larger M and N_Ω as well as a good localization with a larger number of local clusters.

5 Conclusion

We have proposed a multiscale graph-based reduction method for upscaling heterogeneous and anisotropic diffusion problems. The method combines balanced domain decomposition with local spectral clustering to construct multiple coarse-scale variables that effectively capture key local features. Two strategies for the construction of a prolongation operator and the assembly of a coarse-scale system have been developed. Numerical experiments on diverse test cases are presented, including perforated domains, channelized media, strongly anisotropic coefficients, and discrete pore-network models, which confirm the robustness and efficiency of the proposed upscaling framework. We find that the global MC approach yields the most accurate coarse model, even with a single vector and the original subdomains without clustering. In this setting, clustering plays a crucial role in localization and can be used to sparsify the coarse basis when combined with energy minimization. Although the global MC approach requires solving a saddle-point system to construct the energy-minimizing basis, it remains practical with aggressive coarsening and approximate solvers. This suggests that the method warrants further study, particularly with more efficient approximations [40]. For the local approaches, the MC method yields the best results; however, effective localization requires a larger number of local basis functions. By contrast, the CF approach benefits more directly from localization, while the MC approach becomes competitive only for larger numbers of basis functions (clusters and centroids).

Acknowledgments

BSS was supported by the DOE Office of Advanced Scientific Computing Research Applied Mathematics program through Contract No. 89233218CNA000001. LANL report number LA-UR-25-29298.

References

- [1] Oleg Iliev, Raytcho Lazarov, and Joerg Willems. Fast numerical upscaling of heat equation for fibrous materials. *Computing and visualization in science*, 13(6):275, 2010.
- [2] Johannes Reichold, Marco Stampanoni, Anna Lena Keller, Alfred Buck, Patrick Jenny, and Bruno Weber. Vascular graph model to simulate the cerebral blood flow in realistic vascular networks. *Journal of Cerebral Blood Flow & Metabolism*, 29(8):1429–1443, 2009.
- [3] Matthew T Balhoff, Sunil G Thomas, and Mary F Wheeler. Mortar coupling and upscaling of pore-scale models. *Computational Geosciences*, 12:15–27, 2008.
- [4] Jay Chu, Björn Engquist, Maša Prodanović, and Richard Tsai. A multiscale method coupling network and continuum models in porous media i: steady-state single phase flow. *Multiscale Modeling & Simulation*, 10(2):515–549, 2012.
- [5] Andrew T Barker, Chak S Lee, and Panayot S Vassilevski. Spectral upscaling for graph laplacian problems with application to reservoir simulation. *SIAM Journal on Scientific Computing*, 39(5):S323–S346, 2017.
- [6] Gustav Kettil, Axel Målqvist, Andreas Mark, Mats Fredlund, Kenneth Wester, and Fredrik Edelvik. Numerical upscaling of discrete network models. *BIT Numerical Mathematics*, 60:67–92, 2020.
- [7] Morgan Görtz, Fredrik Hellman, and Axel Målqvist. Iterative solution of spatial network models by subspace decomposition. *arXiv preprint arXiv:2207.07488*, 2022.

- [8] George Karypis and Vipin Kumar. Metis: A software package for partitioning unstructured graphs, partitioning meshes, and computing fill-reducing orderings of sparse matrices. 1997.
- [9] Martin J Blunt, Branko Bijeljic, Hu Dong, Oussama Gharbi, Stefan Iglauser, Peyman Mostaghimi, Adriana Paluszny, and Christopher Pentland. Pore-scale imaging and modelling. *Advances in Water resources*, 51:197–216, 2013.
- [10] Yalchin Efendiev, Juan Galvis, and Thomas Y Hou. Generalized multiscale finite element methods (gmsfem). *Journal of computational physics*, 251:116–135, 2013.
- [11] Maria Vasilyeva. Generalized multiscale finite element method for discrete network (graph) models. *Journal of Computational and Applied Mathematics*, 457:116275, 2025.
- [12] Marian Brezina, Andrew J Cleary, Robert D Falgout, Van Emden Henson, Jim E Jones, Thomas A Manteuffel, Stephen F McCormick, and John W Ruge. Algebraic multigrid based on element interpolation (amge). *SIAM Journal on Scientific Computing*, 22(5):1570–1592, 2001.
- [13] Hussam Al Daas and Laura Grigori. A class of efficient locally constructed preconditioners based on coarse spaces. *SIAM Journal on Matrix Analysis and Applications*, 40(1):66–91, 2019.
- [14] Per H. Valvatne and Martin J. Blunt. Predictive pore-scale modeling of two-phase flow in mixed wet media. *Water Resources Research*, 40(7), 2004.
- [15] Jeff T Gostick. Versatile and efficient pore network extraction method using marker-based watershed segmentation. *Physical Review E*, 96(2):023307, 2017.
- [16] Jeff Gostick, Mahmoudreza Aghighi, James Hinebaugh, Tom Tranter, Michael A Hoeh, Harold Day, Brennan Spellacy, Mostafa H Sharqawy, Aimy Bazylak, Alan Burns, et al. Openpnm: a pore network modeling package. *Computing in Science & Engineering*, 18(4):60–74, 2016.
- [17] Grégoire Allaire. Homogenization and two-scale convergence. *SIAM Journal on Mathematical Analysis*, 23(6):1482–1518, 1992.
- [18] Thomas Y Hou and Xiao-Hui Wu. A multiscale finite element method for elliptic problems in composite materials and porous media. *Journal of computational physics*, 134(1):169–189, 1997.
- [19] VE Henson, J Jones, T Manteuffel, S McCormick, and J Ruge. Spectral amge (ρ amge). *SIAM Journal on Scientific Computing*, 25(1):1–26, 2003.
- [20] François Pellegrini and Jean Roman. Scotch: A software package for static mapping by dual recursive bipartitioning of process and architecture graphs. In *High-Performance Computing and Networking: International Conference and Exhibition HPCN EUROPE 1996 Brussels, Belgium, April 15–19, 1996 Proceedings 4*, pages 493–498. Springer, 1996.
- [21] Christophe Geuzaine and Jean-François Remacle. Gmsh: A 3-d finite element mesh generator with built-in pre-and post-processing facilities. *International journal for numerical methods in engineering*, 79(11):1309–1331, 2009.
- [22] Andrew V. Knyazev. On spectral partitioning of signed graphs, 2018.
- [23] Jérôme Kunegis, Stephan Schmidt, Andreas Lommatzsch, Jürgen Lerner, Ernesto W De Luca, and Sahin Albayrak. Spectral analysis of signed graphs for clustering, prediction and visualization. In *Proceedings of the 2010 SIAM international conference on data mining*, pages 559–570. SIAM, 2010.
- [24] Jean Gallier. Spectral theory of unsigned and signed graphs. applications to graph clustering: a survey, 2016.

[25] S. Lloyd. Least squares quantization in pcm. *IEEE Transactions on Information Theory*, 28(2):129–137, 1982.

[26] Andrew Ng, Michael Jordan, and Yair Weiss. On spectral clustering: Analysis and an algorithm. *Advances in neural information processing systems*, 14, 2001.

[27] Jianbo Shi and Jitendra Malik. Normalized cuts and image segmentation. *IEEE Transactions on pattern analysis and machine intelligence*, 22(8):888–905, 2000.

[28] John W Ruge and Klaus Stüben. Algebraic multigrid. In *Multigrid methods*, pages 73–130. SIAM, 1987.

[29] Robert D Falgout and Panayot S Vassilevski. On generalizing the algebraic multigrid framework. *SIAM Journal on Numerical Analysis*, 42(4):1669–1693, 2004.

[30] Thomas A Manteuffel, John Ruge, and Ben S Southworth. Nonsymmetric algebraic multigrid based on local approximate ideal restriction (ℓ air). *SIAM Journal on Scientific Computing*, 40(6):A4105–A4130, 2018.

[31] Thomas A Manteuffel, Steffen Munzenmaier, John Ruge, and Ben Southworth. Nonsymmetric reduction-based algebraic multigrid. *SIAM Journal on Scientific Computing*, 41(5):S242–S268, 2019.

[32] Ahsan Ali, James J Brannick, Karsten Kahl, Oliver A Krzysik, Jacob B Schroder, and Ben S Southworth. Constrained local approximate ideal restriction for advection-diffusion problems. *SIAM Journal on Scientific Computing*, 46(5):S96–S122, 2024.

[33] Jan Mandel and Clark R. Dohrmann. Convergence of a balancing domain decomposition by constraints and energy minimization. *Numerical Linear Algebra with Applications*, 10(7):639–659, 2003.

[34] Artem Napov and Yvan Notay. Algebraic analysis of aggregation-based multigrid. *Numerical Linear Algebra with Applications*, 18(3):539–564, 2011.

[35] Eric T Chung, Yalchin Efendiev, Wing Tat Leung, Maria Vasilyeva, and Yating Wang. Non-local multi-continua upscaling for flows in heterogeneous fractured media. *Journal of Computational Physics*, 372:22–34, 2018.

[36] Maria Vasilyeva, Eric T Chung, Siu Wun Cheung, Yating Wang, and Georgy Prokopev. Nonlocal multi-continua upscaling for multicontinua flow problems in fractured porous media. *Journal of Computational and Applied Mathematics*, 355:258–267, 2019.

[37] Maria Vasilyeva, Eric T Chung, Wing Tat Leung, Yating Wang, and Denis Spiridonov. Upscaling method for problems in perforated domains with non-homogeneous boundary conditions on perforations using non-local multi-continuum method (nlmc). *Journal of Computational and Applied Mathematics*, 357:215–227, 2019.

[38] Golo A. Wimmer, Ben S. Southworth, Koki Sagiyama, and Xian-Zhu Tang. An accurate supg-stabilized continuous galerkin discretization for anisotropic heat flux in magnetic confinement fusion. *The SMAI Journal of Computational Mathematics*, 11:473–496, 2025.

[39] Martin J. Blunt. Flow in porous media — pore-network models and multiphase flow. *Current Opinion in Colloid & Interface Science*, 6(3):197–207, 2001.

[40] Jan Van lent, Robert Scheichl, and Ivan G. Graham. Energy-minimizing coarse spaces for two-level schwarz methods for multiscale pdes. *Numerical Linear Algebra with Applications*, 16(10):775–799, 2009.

[41] Maria Vasilyeva, Golo Wimmer, and Ben S Southworth. Multiscale approximation and two-grid preconditioner for extremely anisotropic heat flow. *Journal of Computational Physics*, 538:114201, 2025.

- [42] Thierry Coulhon and Alexander Grigoryan. Random walks on graphs with regular volume growth. *Geometric and Functional Analysis*, 8(4):656–701, 1998.
- [43] Nadine Badr and José María Martell. Weighted norm inequalities on graphs. *Journal of Geometric Analysis*, 22(4):1173–1210, 2012.
- [44] James Brannick, Scott P MacLachlan, Jacob B Schroder, and Ben S Southworth. The role of energy minimization in algebraic multigrid interpolation. *arXiv preprint arXiv:1902.05157*, 2019.
- [45] Eric T Chung, Yalchin Efendiev, and Wing Tat Leung. Constraint energy minimizing generalized multiscale finite element method. *Computer Methods in Applied Mechanics and Engineering*, 339:298–319, 2018.
- [46] Lina Zhao and Eric T Chung. An analysis of the nlmc upscaling method for high contrast problems. *Journal of Computational and Applied Mathematics*, 367:112480, 2020.
- [47] Tom Manteuffel and Ben S Southworth. Convergence in norm of nonsymmetric algebraic multigrid. *SIAM Journal on Scientific Computing*, 41(5):S269–S296, 2019.
- [48] Klaus Stuben. Algebraic multigrid (amg): an introduction with applications. *GMD report*, 1999.

A Convergence analysis

In this section, we derive convergence estimates for both proposed coarsening approaches. We introduce the discrete weighted norms [11, 41]

$$\|v\|_D^2 = v^T D v = \sum_{i \in \mathcal{V}} d_i v_i^2, \quad \|v\|_L^2 = v^T L v = \sum_{\substack{(i,j) \in \mathcal{E} \\ i,j \in \mathcal{V}}} w_{ij} (v_i - v_j)^2, \quad \|v\|_A^2 = v^T A v.$$

For (12), we have $u_{ms} = P u_c = P(RAP)^{-1} R f$, then

$$u - u_{ms} = u - P(RAP)^{-1} R f = u - P(RAP)^{-1} R A u = (I - P(RAP)^{-1} R A) u = (I - \Pi) u,$$

with $\Pi = P(RAP)^{-1} R A$. We have the Galerkin orthogonality

$$R A (u - u_{ms}) = R (A u - A u_{ms}) = R (f - A u_{ms}) = 0,$$

since $A_c u_c - f_c = R A P u_c - R f = R (A u_{mc} - f) = 0$ and

$$\Pi (u - u_{ms}) = P(RAP)^{-1} R A (u - u_{ms}) = 0.$$

Let $I_k = I_{\Omega_k}^{\Omega_k^+, h} \in \mathbb{R}^{n_k \times n}$ denote the restriction operator onto Ω_k^+ , and $A^{\Omega_k^+} = I_k A I_k^T \in \mathbb{R}^{n_k \times n_i}$, $n_k = |\Omega_k^+|$. With $P = [I_1^T P_1, \dots, I_{N_\Omega}^T P_{N_\Omega}]$, the Galerkin orthogonality is equivalent to the block relations

$$R_k I_k A (u - u_{ms}) = R_k (I_k A I_k^T) I_k (u - u_{ms}) = R_k A^{\Omega_k^+} I_k (u - u_{ms}) = 0, \quad k = 1, \dots, N_\Omega.$$

Then

$$\pi_k (I_k (u - u_{ms})) = 0 \quad \text{with} \quad \pi_k = P_k (R_k A^{\Omega_k^+} P_k)^{-1} R_k A^{\Omega_k^+}.$$

The proposed multiscale method begins by defining coarse variables, which are constructed using local spectral clustering within the non-overlapping subdomains Ω_k (subdomains). Local spectral clustering divide Ω_k into r non-oversampling subsubdomains \mathcal{A}_k^r ($\Omega_k = \bigcup_{r=1}^{M_k} \mathcal{A}_k^r$) and ensures that the contrast of the edge weights w_{ij} , and consequently the degrees d_i , within each local cluster \mathcal{A}_k^r is small.

The bounds for a local cluster \mathcal{A}_k^r define local ratio

$$C_{ratio}^{k,r} = \frac{\bar{d}^{r,k}}{\underline{d}^{r,k}} \approx \frac{\bar{w}^{r,k}}{\underline{w}^{r,k}}, \quad \underline{w}^{k,r} \leq w_{ij} \leq \bar{w}^{k,r}, \quad \underline{d}^{k,r} \leq d_i \leq \bar{d}^{k,r}, \quad i, j \in \mathcal{A}_k^r,$$

where $C_{ratio}^{k,r}$ captures the intra-cluster weight/degree contrast and $d_i = -\sum_j w_{ij}$. For special cases, such as channelized media, we may have $C_{ratio}^{k,r} \approx 1$, indicating that the weights within each cluster are nearly uniform and exhibit similar connectivity patterns. In anisotropic media, the clustering aligns with the anisotropy directions. The choice of M_k (number of local clusters) directly influences the quality of the clustering and the resulting bounds. As M_k increases, each cluster \mathcal{A}_k^r becomes smaller and more homogeneous, leading to smaller values of $C_{ratio}^{k,r}$.

We let $H_{k,r} = \text{diam}(\mathcal{A}_k^r)$ and $C_p > 0$, then using the Poincaré inequality, we obtain

$$\|v\|_{D^{\mathcal{A}_k^r}}^2 \leq \bar{d}^{r,k} \|v\|_k^2 = \underline{d}^{r,k} \frac{\bar{d}^{r,k}}{\underline{d}^{r,k}} \|v\|_k^2 \leq \underline{d}^{r,k} C_{ratio}^{k,r} C_p^2 H_{k,r}^2 \|\nabla v\|_k^2 \leq C_{ratio}^{k,r} C_p^2 H_{k,r}^2 \|v\|_{L^{\mathcal{A}_k^r}}^2, \quad (13)$$

where $\|v\|_k^2 = \sum_{i \in \mathcal{A}_k^r} v_i^2$ and $\|\nabla v\|_k^2 = \sum_{\substack{(i,j) \in \mathcal{E} \\ i,j \in \mathcal{A}_k^r}} (v_i - v_j)^2$ are the unweighted and discrete gradient norms [42, 43]. Then for $\Omega_k = \bigcup_r \mathcal{A}_k^r$, we have [44, 45, 46]

$$\|v\|_{D^{\Omega_k}}^2 \leq C_{ratio}^k C_p^2 H_k^2 \sum_r \|v\|_{L^{\mathcal{A}_k^r}}^2 = C_{ratio}^k C_p^2 H_k^2 \|v\|_{L^{\Omega_k}}^2 \leq C_{ratio}^k C_p^2 H_k^2 \|v\|_{A^{\Omega_k}}^2, \quad (14)$$

with $k_{\min}^k := \min_r k_{\min}^{k,r}$, $C_{ratio}^k = \max_r C_{ratio}^{k,r}$ and $H_k := \max_r H_{k,r}$.

Additionally in CF-approach, we have the following block structure [47, 44]

$$P = \begin{bmatrix} W \\ I \end{bmatrix}, \quad R = \begin{bmatrix} Z & I \end{bmatrix}, \quad A = \begin{bmatrix} A_{ff} & A_{fc} \\ A_{cf} & A_{cc} \end{bmatrix} = \begin{bmatrix} I & 0 \\ A_{cf} A_{ff}^{-1} & I \end{bmatrix} \begin{bmatrix} A_{ff} & 0 \\ 0 & S \end{bmatrix} \begin{bmatrix} I & A_{ff}^{-1} A_{fc} \\ 0 & I \end{bmatrix},$$

with $W = -A_{ff}^{-1} A_{fc}$, $Z = -A_{cf} A_{ff}^{-1}$ and $S = A_{cc} - A_{cf} A_{ff}^{-1} A_{fc}$. Then, we have $RAP = S$ and

$$\Pi = P(RAP)^{-1} RA = \begin{bmatrix} 0 & W \\ 0 & I \end{bmatrix}, \quad \text{then} \quad (I - \Pi)e = \begin{bmatrix} I & -W \\ 0 & 0 \end{bmatrix} \begin{bmatrix} e_f \\ e_c \end{bmatrix} = \begin{bmatrix} e_f - We_c \\ 0 \end{bmatrix}, \quad e = u - u_{ms}.$$

Therefore based on this special structure of the error in CF-approach, we have [48]

$$\|(I - \Pi)e\|_A^2 = e^T A e - e_c^T S e_c \leq \|e\|_A^2, \quad S = A_{cc} - A_{cf} A_{ff}^{-1} A_{fc}.$$

Lemma 1. *Let u be solution of (4) and u_{ms} be a solution of (12), then we have*

$$\|u - u_{ms}\|_D^2 \leq C^2 H^2 C_{ratio} \|u - u_{ms}\|_A^2, \quad (15)$$

with $H = \max_{k,r} H_{k,r}$ and $C_{ratio} = \max_{k,r} C_{ratio}^{k,r}$.

Proof. Since the subdomains $\{\Omega_k\}$ are non-overlapping and based on the Galerkin orthogonality, we have

$$\|u - u_{ms}\|_D^2 = \|e\|_D^2 = \sum_{k=1}^{N_\Omega} \|e_k\|_{D^{\Omega_k^+}}^2 = \sum_{k=1}^{N_\Omega} \|(I - \pi_k)e_k\|_{D^{\Omega_k^+}}^2 = \sum_{k=1}^{N_\Omega} \|r_k\|_{D^{\Omega_k^+}}^2,$$

with $e = u - u_{ms}$, $e_k = I_k e$ and $r_k = (I - \pi_k)e_k$.

For the CF-approach, we have

$$\sum_{k=1}^{N_\Omega} \|r_k\|_{D^{\Omega_k^+}}^2 = \sum_{k=1}^{N_\Omega} \sum_{j=1}^{\Omega_j \in \Omega_k^+} \|r_k\|_{D^{\Omega_j}}^2 \leq C_o \sum_{k=1}^{N_\Omega} \|r_k\|_{D^{\Omega_k}}^2$$

where C_o depends on the maximum number of overlapping subdomains sharing the same Ω_k .
With the MC approach and the basis construction constraints, we obtain [45, 46]

$$\sum_{k=1}^{N_\Omega} \|r_k\|_{D^{\Omega_k^+}}^2 = \sum_{k=1}^{N_\Omega} \|r_k\|_{D^{\Omega_k}}^2$$

Then using the local estimate (14) on each Ω_k , we obtain

$$\|e\|_D^2 \leq C_o \sum_{i=1}^{N_\Omega} C_{ratio}^k C_p^2 H_k^2 \|r_k\|_{A^{\Omega_k}}^2 \leq C^2 H^2 C_{ratio} \|r\|_A^2 \leq C^2 H^2 C_{ratio} \|e\|_A^2,$$

with $C^2 = C_o C_p^2$ ($C_o = 1$ in MC-approach), $H = \max_k H_k$ and $C_{ratio} = \max_k C_{ratio}^k$. \square

Theorem 1. *Let u be solution of (4) and u_{ms} be a solution of (12), then we have*

$$\|u - u_{ms}\|_A \leq CHC_{ratio}^{1/2} \|f\|_{D^{-1}}. \quad (16)$$

Proof. Based on (4) and (12) with $A = A^T$, $R = P^T$, we have

$$(u - u_{ms})^T A u_{ms} = (Au)^T P u_c - u_c^T R A P u_c = (Au)^T P u_c - u_c^T R f = (Au)^T P u_c - (P u_c)^T f = 0.$$

Therefore using the Cauchy–Schwarz inequality, we obtain

$$\|u - u_{ms}\|_A^2 = (u - u_{ms})^T A (u - u_{ms}) = (u - u_{ms})^T A u = (u - u_{ms})^T f \leq \|f\|_{D^{-1}} \|u - u_{ms}\|_D.$$

Finally using the Lemma 1, we get

$$\|u - u_{ms}\|_A^2 \leq \|f\|_{D^{-1}} \|u - u_{ms}\|_D \leq \|f\|_{D^{-1}} CHC_{ratio}^{1/2} \|u - u_{ms}\|_A.$$

\square